photonics

MDPI

Article

Luminescence Efficiency of Tm^{3+}-Doped Crystals at 2.0 μm Under 793 nm Excitation

Mohan Wang [1,2], Lu Zhang [2,3], Yachen Gao [1,*] and Zhiguo Zhang [2,4,*]

1 School of Electronic Engineering, Heilongjiang University, Harbin 150080, China; 20232125@s.hlju.edu.cn
2 Functional Crystal Materials, Xinjiang Technical Institute of Physics and Chemistry, Chinese Academy of Sciences, 40-1 South Beijing Road, Urumqi 830011, China; zhanglu199951@hrbeu.edu.cn
3 College of Physics and Optoelectronic Engineering, Harbin Engineering University, Harbin 150001, China
4 School of Instrumentation Science and Engineering, Harbin Institute of Technology, Harbin 150001, China
* Correspondence: gaoyachen@hlju.edu.cn (Y.G.); zhangzhiguo@hit.edu.cn (Z.Z.)

Abstract

This study investigates the 2.0 μm luminescence efficiency of Tm^{3+}-doped crystals under 793 nm excitation. An analytical model decomposing laser slope efficiency into the quantum defect, fluorescence quantum efficiency (η_q), and a mode matching factor was established, highlighting η_q optimization as key. Using a high-precision spectral system, the comparative study of Tm:YAG and Tm:YAP crystals revealed unprecedented η_q values of 184.8% and 190.6%, respectively. This breakthrough, corroborated by double-exponential decay kinetics, verifies the cross-relaxation-dominated quantum cutting mechanism. Superior performance of Tm:YAP crystal is attributed to its lower phonon energy, effectively suppressing non-radiative losses, providing a foundation for high-performance 2.0 μm lasers.

Keywords: Tm^{3+}-doped crystals; 2.0 μm luminescence; fluorescence quantum efficiency; 793 nm excitation; cross-relaxation; Tm:YAG; Tm:YAP

1. Introduction

The development of efficient ~2.0 μm lasers is critical for applications, with pioneering spectroscopic and laser investigations of Tm^{3+}-doped crystals laying the foundation for the entire field [1]; their key applications include lidar [2], surgery [3], and mid-infrared generation. Tm^{3+}-doped crystals are ideal gain media for this band due to the intrinsic $^3F_4 \rightarrow {}^3H_6$ transition [4]. Beyond conventional Tm:YAG and Tm:YAP crystals, novel mixed rare-earth aluminate crystals have emerged as promising gain media for high-performance 2 μm lasers [5]. In practice, optimizing such lasers often relies on empirical tuning, creating a need for a definitive performance criterion. This criterion is provided by laser physics, which defines the slope efficiency η_{slope} for a quasi-three-level system as being proportional to the product of the fluorescence quantum efficiency η_q and the mode matching factor k, i.e., $\eta_{slope} \propto \eta_q \times k$ [6]. When η_q is known, the measured η_{slope} directly yields the achieved κ value, which quantifies the pump-to-laser mode overlap and precisely indicates the direction for further optical alignment optimization. Therefore, an accurate measurement of η_q is paramount, as it provides the essential benchmark for effectively guiding the laser development process.

The pursuit of efficient ~2.0 μm lasers necessitates the accurate determination of the fluorescence quantum efficiency η_q of the gain medium. The methodologies for measuring η_q can be broadly categorized into absolute and relative methods. The mainstream and most reliable approach for obtaining absolute η_q values involves using an integrating

Check for updates

Received: 1 April 2026
Revised: 28 April 2026
Accepted: 1 May 2026
Published: 8 May 2026

Copyright: © 2026 by the authors. Licensee MDPI, Basel, Switzerland. This article is an open access article distributed under the terms and conditions of the Creative Commons Attribution (CC BY) license.

sphere coupled with a spectrometer [7]. This technique directly compares the total number of photons absorbed by the sample to the total number of photons emitted across the fluorescence band, providing a model-independent measurement. The accuracy of such absolute measurements is highly dependent on the performance of the detection system. In the visible spectrum, where silicon-based detectors offer high sensitivity and excellent linearity, this method yields highly reliable results. Consequently, a well-established database of η_q exists for visible-wavelength emitters. In stark contrast, measurements in the near-infrared region, particularly around 2.0 μm, still face significant technical challenges, which has become a key bottleneck restricting the development of high-performance Tm^{3+}-doped 2 μm lasers [8]. The performance of detectors like InGaAs declines, exhibiting lower sensitivity and higher noise, which substantially increases the uncertainty of the measured η_q values. Given these instrumentation limitations, simpler approaches based solely on spectroscopic analysis are sometimes considered. However, for highly doped Tm^{3+} systems where complex energy transfer processes dominate, such indirect methods are generally insufficient for capturing the actual efficiency governed by ion–ion interactions.

This work systematically investigates the ~2.0 μm fluorescence efficiency of Tm^{3+}-doped crystals under 793 nm excitation to enhance ~2.0 μm laser performance [9]. Theoretically, Judd–Ofelt theory and energy transfer dynamics elucidate the cross-relaxation-dominated quantum cutting mechanism. Experimentally, an absolute measurement method using a standard lamp-calibrated spectrometer was devised for the comparative study of Tm:YAG and Tm:YAP crystals. The results show exceptionally high η_q values of 184.8% and 190.6%, which, combined with double-exponential decay kinetics, directly verify the quantum cutting effect and attribute the superior performance of Tm:YAP crystal to its lower phonon energy [10].

2. Theoretical Foundation and Research Methods

2.1. Decomposition Model and Analytical Framework of Laser Efficiency

Based on the rate equation theory of quasi-three-level laser systems [11], the slope efficiency and output characteristics have been widely investigated in various Tm^{3+}-doped laser configurations including slab lasers. This framework references the classical laser physics theory system, with its core mathematical expression as [6]:

$$\eta_{\text{slope}} = (\lambda_p/\lambda_l) \times \eta_q \times k \quad (1)$$

In this theory, k is the mode matching factor, which is a dimensionless parameter describing the spatial overlap efficiency between the pump light field and the laser oscillation mode in the gain medium. η_{slope} is the slope efficiency of the laser, a core indicator measuring energy conversion performance. λ_p and λ_l are the wavelengths of the pump light and laser, respectively; their ratio of λ_p/λ_l is approximately 0.4. This term is called the "quantum defect", inherently determined by the energy level structure of the Tm^{3+} ion itself reflecting the unavoidable Stokes shift loss in the energy conversion process, setting a physical boundary for laser efficiency optimization.

The fluorescence quantum efficiency, characterized here as η_q, measures the probability that pump photons absorbed by the gain medium are ultimately converted into fluorescence photons that can participate in laser output. In the highly Tm^{3+}-doped systems, the specific value of η_q is influenced by various energy transfer processes. Among them, the cross-relaxation process between Tm^{3+} ions may induce a quantum cutting effect; theoretically, this effect could allow η_q to exceed 100%. However, in actual highly doped systems, loss processes such as energy up-conversion and excited-state absorption are prevalent, significantly reducing the measured η_q.

The mode matching factor, represented by parameter k, quantitatively describes the spatial overlap between the pump light and the laser mode within the gain medium. Under ideal experimental conditions, when k equals 1, all pump energy absorbed by the medium contributes to laser gain. But in practical laser systems, factors such as the quality of the pump beam itself, thermal lensing effects during operation, and the design of the resonator cavity cause k to be less than the ideal value. Therefore, optimizing k is a systems engineering task involving multiple aspects.

Given that the quantum defect remains essentially constant, the optimization direction for improving laser output efficiency primarily revolves around the two core parameters η_q and k. This systematic approach to efficiency optimization addresses a key challenge in advancing mid-infrared laser technology [12]. Similar approaches to efficiency decomposition and loss management have also been demonstrated in recent laser system studies [13].

2.2. Spectral Quantification and Calibration Method

The key to obtaining the absolute value of the fluorescence quantum efficiency η_q lies in converting the spectrometer's relative signal into an absolute photon flux. The calibration method used in this study, based on a standard lamp, aims to establish the spectral response function $R(\lambda)$ of the detection system.

A calibrated standard tungsten ribbon lamp, whose spectral irradiance $F_{std}(\lambda)$ is given by Planck's blackbody radiation law, is used for calibration. The system's response function is calculated by measuring the lamp's signal $I_{std}(\lambda)$ under identical conditions [14]:

$$R(\lambda) = I_{std}(\lambda)/F_{std}(\lambda) \tag{2}$$

The raw fluorescence signal from the sample $I_{raw}(\lambda)$ is then corrected for dark background $I_{dark}(\lambda)$ and divided by $R(\lambda)$ to obtain the absolute spectral irradiance $I_{abs}(\lambda)$ at the monochromator entrance:

$$I_{abs}(\lambda) = (I_{raw}(\lambda) - I_{dark}(\lambda))/R(\lambda) \tag{3}$$

For quantum efficiency calculation, the energy distribution must be converted to a photon number distribution. The photon flux $Q(\lambda)$ is given by:

$$Q(\lambda) = I_{abs}(\lambda) \cdot \lambda/(hc) \tag{4}$$

where h is Planck's constant and c is the speed of light. Integrating $Q(\lambda)$ over the fluorescence band yields the total emitted photon number N_{emit}. The η_q is then calculated as N_{emit}/N_{abs}.

2.3. Energy Transfer Dynamics Theory

Energy transfer dynamics is the key theoretical basis for understanding the luminescence characteristics and laser performance of highly Tm^{3+}-doped crystals [15]. In this system, energy transfer processes not only determine the magnitude of the fluorescence quantum efficiency but also directly affect various aspects of laser performance. Analyzing the physical mechanisms, the energy transfer in the Tm^{3+}-doped system mainly involves interactions between ions, which can be divided into short-range exchange interactions and long-range multipole interactions based on distance dependence.

These interactions can be divided into short-range exchange interactions and long-range multipole interactions based on distance dependence. In typical highly Tm^{3+}-doped systems, since the 4f electrons of rare-earth ions are shielded by outer electrons, the interac-

tion is predominantly dipole–dipole [16]. The rate of this process can be described by the Förster–Dexter theory, with the general form being [17]

$$W_{ET} = \frac{C_{DA}}{R^n} \tag{5}$$

where C_{DA} is the microparameter representing the interaction strength between donor (D) and acceptor (A) ions, R is the distance between the interacting ion pair, and n is an integer (6, 8, 10) depending on the multipole order of the interaction (dipole–dipole, dipole–quadrupole, etc.). In highly Tm^{3+}-doped systems, the energy transfer kinetics are dominated by various transition mechanisms between energy levels, which crucially determine the fluorescence quantum efficiency. As shown in Figure 1, under 793 nm excitation, Tm^{3+} ions may undergo several distinct pathways. Mechanisms ① and ② represent the basic excitation and emission cycle, where one absorbed pump photon produces one target ~2.0 μm photon. Mechanisms ③ and ④ consume pump energy but do not generate the desired photons, acting as loss paths. Mechanisms ⑤ and ⑥ depict the cross-relaxation energy transfer ($^3H_4 + {}^3H_6 \rightarrow {}^3F_4 + {}^3F_4$), which is a quantum cutting process capable of generating two target photons from a single pump photon, thereby theoretically enabling η_q to exceed 200%.

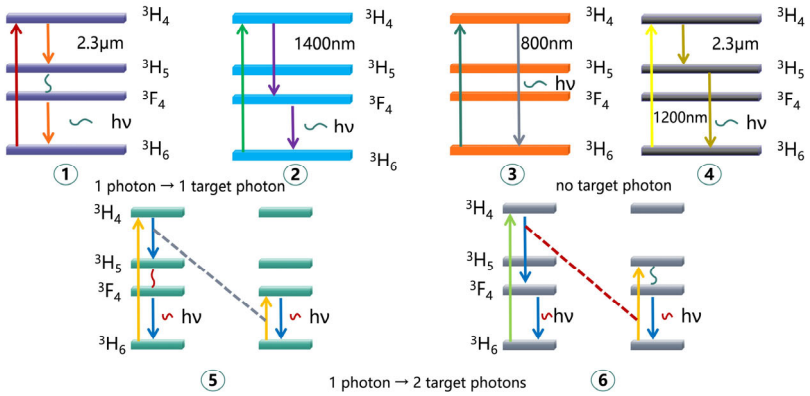


Figure 1. Several transition mechanisms of Tm^{3+} ions.

2.4. Estimation of Non-Radiative Relaxation from Energy Levels

The energy decay of excited ions includes both radiative transitions and non-radiative relaxation. The non-radiative relaxation probability W_{nr} is critical for the fluorescence quantum efficiency η_q, as defined by

$$\eta_q = A_r / (A_r + W_{nr}) \tag{6}$$

where A_r is the radiative transition rate (or Einstein A coefficient) from the emitting energy level. The non-radiative relaxation probability W_{nr} from the $^3F_4$ level of Tm^{3+} ions can be estimated using the energy gap law [15]. An approximate form of this law is:

$$W_{nr} \propto exp(-\alpha \frac{\Delta E}{\hbar \omega_{max}}) \tag{7}$$

where ΔE is the energy gap to the next lower level, and $\hbar\omega_{max}$ is the maximum phonon energy of the host crystal. This indicates that a larger energy gap or a lower host phonon energy results in a smaller W_{nr}.

Thus, the choice of host matrix is crucial for suppressing non-radiative losses. For instance, the maximum phonon energy of YAP ($YAlO_3$, ~600 cm^{-1}) is lower than that of YAG ($Y_3Al_5O_{12}$, ~700 cm^{-1}). According to the energy gap law, the W_{nr} in Tm:YAP is

expected to be lower than in Tm:YAG, providing a theoretical basis for its observed higher fluorescence efficiency. This underscores a fundamental principle in the design of rare-earth-doped lasers: the host matrix's phonon energy is a key determinant of performance, a factor extensively analyzed in comparative studies of Tm^{3+} and Ho^{3+} materials [18].

3. Experimental Section and Optimization Scheme

3.1. Experimental Design and Research Plan

Building upon the theoretical analysis framework established in previous chapters, this study designed a systematic and complete experimental plan. The research focus was centered on the spectral response characteristics and energy transfer mechanisms of Tm^{3+}-doped crystals. The experiment adopted a comparative research method as the core approach, using Tm:YAG (Tm^{3+} doping concentration of 3 mol%) and Tm:YAP (Tm^{3+} doping concentration of 5 mol%) crystals as specific research objects. These crystals were purchased by the Shanghai Institute of Optics and Fine Mechanics of the Chinese Academy of Sciences. Through precise spectral testing and data analysis, we aimed to uncover the core factors affecting infrared fluorescence efficiency.

This experiment established a high-precision independent spectral test system. The core components of the system included a 793 nm semiconductor laser, a triple-grating monochromator, and a liquid nitrogen-cooled InGaAs detector. The output power of the laser was adjusted from 0 to 40 W, the output wavelength of the laser was 793 nm, which was measured by a Maya2000pro Spectrometer which was purchased by the Shanghai Institute of Optics and Fine Mechanics of the Chinese Academy of Sciences. (wavelength range of 190–1100 nm, and the error range is 0.2 nm), and a monochromator with spectral resolution of 0.1 nm measured the emission spectrum of thulium ion-doped crystal. The optical path of the spectral test system is shown in Figure 2. The design employed an orthogonal detection geometry structure, effectively suppressing stray light interference. The pump light was focused by a lens group, achieving good matching with the laser mode spot. The fluorescence signal collection system adopted an f/4 optical design, ensuring high light throughput collection efficiency and providing a guarantee for accurate detection of fluorescence signals. The orthogonal geometry is a standard design for reducing scattered light artifacts in fluorescence spectroscopy [19].

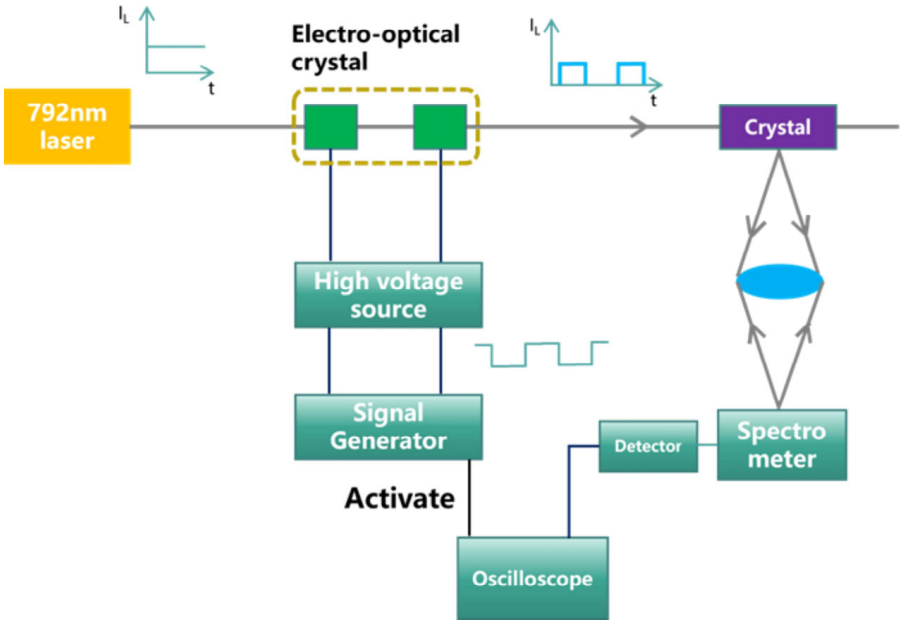


Figure 2. Schematic diagram of the optical path for measuring crystal fluorescence spectra.

To ensure measurement accuracy, the experiment employed a two-level calibration method. First, a NIST-traceable standard tungsten lamp was used to calibrate the system response, establishing a wavelength-sensitivity correction curve. During the calibration process, the standard lamp was measured under identical experimental conditions, and the system response function was calculated through blackbody radiation theory: The use of standard lamps for absolute radiometric calibration is a fundamental practice in quantitative spectroscopy, traceable to international standards [20].

$$R(\lambda) = \frac{I_{\text{std}}(\lambda)}{F_{\text{std}}(\lambda)} \tag{8}$$

where $I_{\text{std}}(\lambda)$ is the measurement signal of the standard lamp, and $F_{\text{std}}(\lambda)$ is its standard irradiance value. After obtaining the system response function, the relative fluorescence intensity of the sample was converted to absolute intensity using:

$$I_{\text{abs}}(\lambda) = \frac{I_{\text{meas}}(\lambda)}{R(\lambda)} \tag{9}$$

To verify the validity of the calibration process and the stability of the detection system, the emission spectrum of the NIST-traceable standard tungsten ribbon lamp was recorded under the exact same experimental conditions as the sample measurement, as shown in Figure 3. The measured spectrum is highly consistent with the theoretical blackbody radiation curve of the standard lamp, which confirms the reliability of the system response function established in this work.

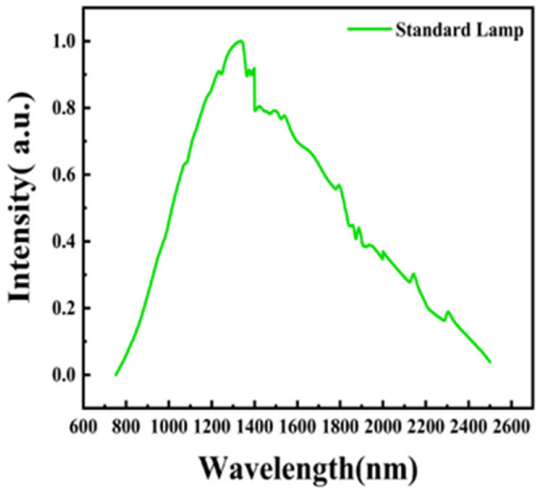


Figure 3. Measured emission spectrum of the NIST-traceable standard tungsten ribbon lamp used for system spectral calibration.

During the experiment, special attention was paid to the optimization of measurement parameters. The monochromator slit width was set to 100 μm, corresponding to a spectral resolution of 0.1 nm. The scanning step was set to 0.05 nm, and the integration time was adaptively adjusted between 0.1 and 1 s according to signal intensity. This parameter setting ensured both measurement efficiency and data quality.

3.2. Data Processing and Efficiency Calculation Method

After obtaining the original spectral data, a strict data processing flow was adopted to ensure result reliability. The fluorescence spectrum is shown in Figure 4. Data processing mainly included four steps: original data preprocessing, system response correction, photon number conversion, and efficiency calculation. Such comprehensive data processing

pipelines are critical for converting raw spectral data into meaningful physical quantities like photon numbers and quantum efficiencies [19].

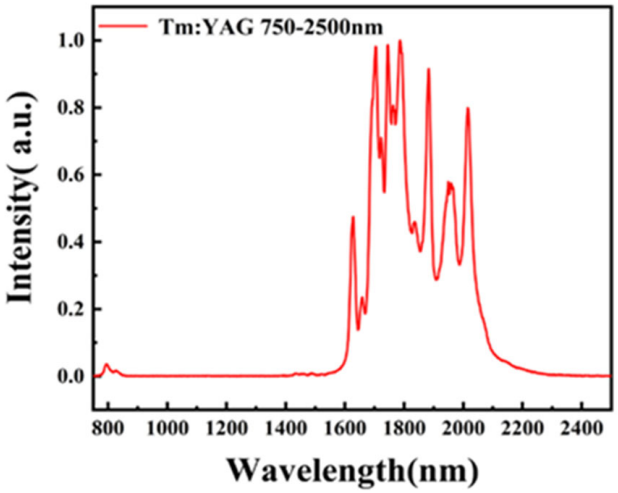


Figure 4. Fluorescence spectrum of a Tm:YAG (Tm^{3+} doping concentration of 3 mol %) crystal in the 780–2500 nm range upon 793 nm laser excitation.

System response correction was key to ensuring data accuracy. Based on the previously obtained system response function R(λ), measurement data were corrected. Particular attention was paid to handling nonlinear effects during correction, using piecewise linear interpolation methods to ensure correction accuracy. The corrected light intensity data was expressed as:

$$I_{\text{corr}}(\lambda) = \frac{I_{\text{raw}}(\lambda) - I_{\text{dark}}(\lambda)}{R(\lambda)} \tag{10}$$

Photon number distribution conversion employed the following formula:

$$Q(\lambda) = \frac{I_{\text{corr}}(\lambda) \times \lambda}{h \times c} \tag{11}$$

This conversion eliminated wavelength-dependent detection efficiency differences, making luminescence intensities at different wavelengths comparable. During conversion, numerical integration methods were used to calculate photon numbers for each band, with integration intervals dynamically adjusted according to fluorescence peak shapes. Fluorescence quantum efficiency calculation was based on the photon number integration method. The characteristic fluorescence peak of Tm^{3+} around 2.0 μm was integrated, with the integration interval set to 1800–2200 nm. The total emitted photon number was calculated as:

$$N_{\text{emit}} = \int_{\lambda_1}^{\lambda_2} Q_{\text{emit}}(\lambda) d\lambda \tag{12}$$

The absorbed photon number was calculated through absorption spectroscopy:

$$N_{\text{abs}} = \frac{\lambda_p}{hc} \int I_{\text{abs}}(\lambda) d\lambda \tag{13}$$

Finally, the fluorescence quantum efficiency was:

$$\eta_q = \frac{N_{\text{emit}}}{N_{\text{abs}}} \tag{14}$$

To evaluate cross-relaxation efficiency, time-resolved fluorescence technology was employed. Fluorescence decay curves were measured and fitted using nonlinear least squares methods to extract decay time constants. The fitting function was:

$$I(t) = A_1 \exp\left(-\frac{t}{\tau_1}\right) + A_2 \exp\left(-\frac{t}{\tau_2}\right) + I_0 \quad (15)$$

where τ_1 and τ_2 are the fast and slow decay time constants, respectively, and A_1, A_2 are their corresponding amplitudes. I_0 is a constant background. By analyzing the amplitude ratio A_2/A_1 of decay components, the contribution degree of cross-relaxation processes was evaluated. This method provided an important basis for understanding energy transfer mechanisms [21].

4. Results and Discussion

4.1. Indication of Luminescence Mechanism

This study conducted systematic spectroscopic tests on Tm:YAG and Tm:YAP crystals and successfully obtained their complete spectral characteristic data. Absorption spectroscopy results showed that Tm^{3+} ions have strong absorption peaks at the 793 nm wavelength. As shown in Figure 5 (right), the rigorously calibrated photon number spectrum of the Tm:YAG crystal exhibits a series of sharp, discrete emission peaks within the 1700–1950 nm interval, which is the characteristic signature of the $^3F_4 \rightarrow {}^3H_6$ transition. The spectrum is explicitly annotated with a light-to-light conversion efficiency as high as 184.8%. This quantum efficiency, significantly exceeding 100%, provides the most direct experimental evidence for the quantum cutting mechanism dominated by the cross-relaxation process between Tm^{3+} ions ($^3H_4 + {}^3H_6 \rightarrow {}^3F_4 + {}^3F_4$). It indicates that a single absorbed 793 nm pump photon, through efficient energy transfer, ultimately generates more than one ~2.0 μm fluorescence photon.

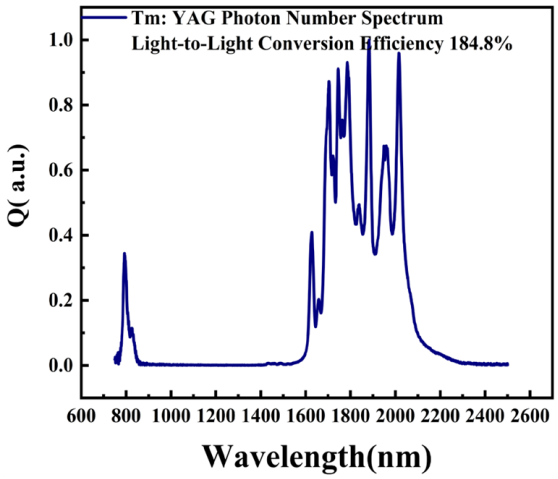


Figure 5. Calculation of the optical-to-optical conversion efficiency for the Tm:YAG (Tm^{3+} doping concentration of 3 mol %) crystal.

4.2. Spectral Calibration

To ensure the absolute accuracy of the measurement results, a rigorous data processing protocol, as detailed in Section 3.2, was employed. All measured fluorescence spectra underwent system response calibration and conversion to photon number distributions. This procedure eliminates the spectral response variations of the instrument and yields absolute photon number distributions that can be directly compared with theory. As shown in Figure 6, the calibrated photon number spectrum of the Tm:YAP (Tm^{3+} doping

concentration of 5 mol %) crystal is clearly discernible across the 780–2500 nm range. The characteristics of the curve, such as peak positions and spectral shape, serve as direct evidence for assessing spectral quality and the validity of the calibration. This calibration process is the fundamental prerequisite for the subsequent precise calculation of the fluorescence quantum yield.

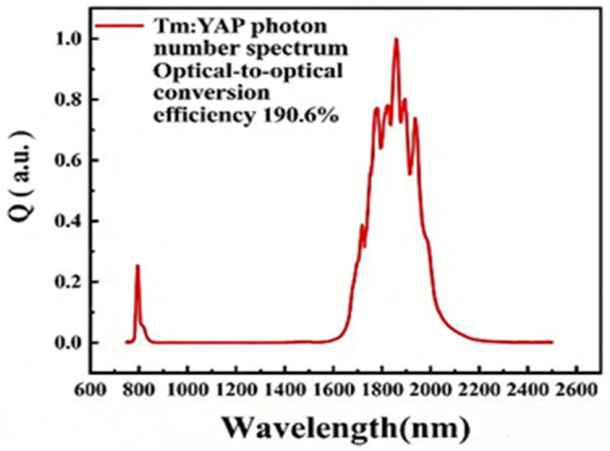


Figure 6. Photon number distribution of Tm:YAP (Tm^{3+} doping concentration of 5mol %) at 780–2500 nm).

4.3. Determination of Quantum Yield

Based on the calibrated spectral data, the fluorescence quantum efficiency η_q was calculated using the photon number integration method. The results show that the η_q value for the Tm:YAG (Tm^{3+} doping concentration of 3 mol %) crystal reached 184.8%, while that for the Tm:YAP (Tm^{3+} doping concentration of 5 mol %) crystal was as high as 190.6%. Both values significantly exceed the conventional theoretical limit of 100%, providing the most direct quantitative evidence for the quantum cutting effect dominated by the cross-relaxation process between Tm^{3+} ions. This represents a notable advancement in the field of mid-infrared laser materials.

Comparing the performance of the two crystals with different host matrices, the YAP matrix demonstrates superior comprehensive performance. Its higher η_q value is primarily attributed to the lower phonon energy of the YAP host (approximately 600 cm^{-1} for YAP vs. 700 cm^{-1} for YAG) [22], which effectively suppresses energy loss caused by non-radiative relaxation, and the lower lattice symmetry of the YAP matrix, which is beneficial for improving the radiative transition probability of the Tm^{3+} ions. These properties work in concert to contribute to its more efficient fluorescence output within the YAP host matrix.

5. Conclusions

This study demonstrates a comprehensive strategy to enhance the 2.0 μm laser efficiency in Tm^{3+}-doped crystals. We established a model decomposing slope efficiency into the quantum defect, fluorescence quantum efficiency η_q, and mode matching factor, highlighting the optimization of η_q as the key pathway. An absolute measurement method was developed to accurately determine η_q yielding breakthrough values of 184.8% for Tm:YAG (Tm^{3+} doping concentration of 3 mol %) and 190.6% for Tm:YAP (Tm^{3+} doping concentration of 5 mol %), which significantly surpass the conventional 100% limit. This ultra-efficiency, verified by time-resolved spectroscopy, originates from a cross-relaxation-induced quantum cutting effect [23]. The superior performance of Tm:YAP is attributed to its lower phonon energy, which effectively suppresses non-radiative loss. Our work provides a solid foundation for developing high-performance 2.0 μm lasers based on

Tm^{3+}-doped crystals. The exceptionally high η_q values demonstrated here are particularly advantageous for power-scalable architectures like the rapidly evolving thin-disk lasers operating in this spectral region. Future work will incorporate thermal management and explore more crystal matrices [24,25].

Author Contributions: Conceptualization, Z.Z.; methodology, Z.Z.; software, M.W. and L.Z.; validation M.W. and L.Z.; formal analysis, M.W. and L.Z.; investigation, M.W. and L.Z.; data curation, M.W. and L.Z.; writing—original draft preparation, M.W.; writing—review and editing, M.W.; visualization, Z.Z.; supervision, Z.Z. and Y.G.; project administration, Z.Z. and Y.G.; funding acquisition, Z.Z. and Y.G. All authors have read and agreed to the published version of the manuscript.

Funding: The Project is Supported by the Science and Technology Innovation Climbing Program of Harbin Normal University (XKB202306); Key Research and Development Plan of Xinjiang Uygur Autonomous Region (2022B01040, 2022B01040-2); Key project of Heilongjiang Natural Science Foundation (ZD2021F002).

Data Availability Statement: The original contributions presented in this study are included in the article. Further inquiries can be directed to the corresponding authors.

Conflicts of Interest: The authors declare no conflicts of interest.

References

1. Bagayev, S.N.; Vatnik, S.M.; Maiorov, A.P.; Pavlyuk, A.A.; Plakushchev, D.V. The spectroscopy and lasing of monoclinic Tm:KY(WO4)$_2$ crystals. *Quantum Electron.* **2000**, *30*, 310. [CrossRef]
2. Spinhirne, J.D. Micro pulse lidar. *IEEE Trans. Geosci. Remote Sens.* **1993**, *31*, 48–55. [CrossRef]
3. Ha, L.; Jaspan, M.; Welford, D.; Evers, M.; Kositratna, G.; Casper, M.J.; Manstein, D.; Birngruber, R. First assessment of a carbon monoxide laser and a thulium fiber laser for fractional ablation of skin. *Lasers Surg. Med.* **2020**, *52*, 788–798. [CrossRef]
4. Pollnau, M.; Eichhorn, M. Spectral coherence, Part I: Passive-resonator linewidth, fundamental laser linewidth, and Schawlow-Townes approximation. *Prog. Quantum Electron.* **2020**, *72*, 100255. [CrossRef]
5. Chen, Q.; Chen, Y.; Zhang, P.; Li, Z.; Yang, Q.; Hang, Y.; Chen, Z. Crystal growth, spectra properties, and 2-μm laser performance of a novel 'mixed' Tm^{3+}-doped $CaY_{0.65}Gd_{0.35}AlO_4$ crystal. *J. Alloys Compd.* **2022**, *928*, 167174. [CrossRef]
6. Koechner, W. *Solid-State Laser Engineering*, 6th ed.; Springer: New York, NY, USA, 2006.
7. Jia, Z.; Pu, C.; Ren, L. Study on Absolute Measurement Method of Fluorescence Quantum Efficiency. *Metrol. Sci. Technol.* **2022**, *66*, 17–22.
8. Ma, X.; Zhang, M.; Wang, T.; Li, X.; Zhu, X.; Wang, Z.; Zhang, J.; Jia, Z.; Tao, X. Synergistic integration of disordered Tm:$CaGdAlO_4$ single-crystal fibers with oxidation-resistant MXene for high-performance 2 μm lasers. *J. Mater. Chem. C* **2026**, *14*, 7266–7274. [CrossRef]
9. Jackson, S.D. Towards high-power mid-infrared emission from a fibre laser. *Nat. Photonics* **2012**, *6*, 423–431. [CrossRef]
10. Duan, X.M.; Ding, Y.; Dai, T.Y.; Zhao, K.; Yao, B.Q. Experimental study of a VBG-based Tm:YLF slab laser at different output coupler parameters. *Quantum Electron.* **2015**, *45*, 312. [CrossRef]
11. Eichhorn, M. Quasi-three-level solid-state lasers in the near and mid infrared based on trivalent rare-earth ions. *Appl. Phys. B* **2008**, *93*, 269–316. [CrossRef]
12. Tomilov, S.; Hoffmann, M.; Wang, Y.; Saraceno, C.J. Moving towards high-power thin-disk lasers in the 2 μm wavelength range. *J. Phys. Photonics* **2021**, *3*, 022002. [CrossRef]
13. Khurgin, J.B.; Pruessner, M.W.; Stievater, T.H.; Rabinovich, W.S. Laser-Rate-Equation Description of Optomechanical Oscillators. *Phys. Rev. Lett.* **2012**, *108*, 223904. [CrossRef] [PubMed]
14. Da Vila, L.D.; Gomes, L.; Tarelho, L.V.G.; Ribeiro, S.J.L.; Messaddeq, Y. Dynamics of Tm-Ho energy transfer and deactivation of the $^3F_4$ low level of thulium in fluorozirconate glasses. *J. Appl. Phys.* **2004**, *95*, 5451–5463. [CrossRef]
15. Zhang, X.L.; Wang, Y.Z. Influence of energy transfer upconversion on the upper-level lifetime of Tm, Ho:YLF Q-switched laser. *Acta Phys. Sin.* **2006**, *55*, 1160–1164. [CrossRef]
16. Jackson, S.D. The spectroscopic and energy transfer characteristics of the rare earth ions used for silicate glass fibre lasers operating in the shortwave infrared. *Laser Photon. Rev.* **2009**, *3*, 466–482. [CrossRef]
17. Dexter, D.L. A Theory of Sensitized Luminescence in Solids. *J. Chem. Phys.* **1953**, *21*, 836–850. [CrossRef]
18. Walsh, B.M. Review of Tm and Ho materials: Spectroscopy and lasers. *Laser Photonics Rev.* **2016**, *10*, 895–936. [CrossRef]
19. Walsh, B.M.; Grew, G.W.; Barnes, N.P. Energy levels and intensity parameters of Ho^{3+} ions in $GdLiF_4$, $YLiF_4$ and $LuLiF_4$. *J. Phys. Condens. Matter* **2005**, *17*, 7643–7665. [CrossRef]

20. Dai, C.; Wang, Y.; Li, L.; Wu, Z.; Xie, Y.; Khlevnoy, B.; Grigoryeva, I.; He, S.; Lin, Y. Spectral irradiance scale realization and uncertainty analysis based on a 14 mm diameter WC–C fixed point blackbody from 250 nm to 2500 nm. *Metrologia* **2022**, *59*, 024001. [CrossRef]
21. Jiang, Q.; Zhang, L.; Wang, H.; Yang, X.; Meng, J.; Liu, H.; Yin, Z.; Wu, J.; Zhang, X.; You, J. Enhanced electron extraction using SnO_2 for high-efficiency planar-structure $HC(NH_2)2PbI_3$-based perovskite solar cells. *Nat. Energy* **2017**, *2*, 16177. Correction in *Nat. Energy* **2017**, *2*, 17060. https://doi.org/10.1038/nenergy.2017.60. [CrossRef]
22. Walsh, B.M.; Barnes, N.P.; Petros, M.; Yu, J.; Singh, U.N. Spectroscopy and modeling of solid state lanthanide lasers: Application to trivalent Tm^{3+} and Ho^{3+} in $YLiF_4$ and $LuLiF_4$. *J. Appl. Phys.* **2004**, *95*, 3255–3271. [CrossRef]
23. Sun, C.; Liu, J.; Gong, Y.; Wilkinson, D.P.; Zhang, J. Recent advances in all-solid-state rechargeable lithium batteries. *Nano Energy* **2017**, *33*, 363–386. [CrossRef]
24. Mao, J.; Liu, Z.; Zhou, J.; Zhu, H.; Zhang, Q.; Chen, G.; Ren, Z. Advances in thermoelectrics. *Adv. Phys.* **2018**, *67*, 69–147. [CrossRef]
25. Farah Asyiqa, A.; Yusof, N.; Iskandar, S.; Hisam, R.; Azlan, M.; Zaid, M.; Yusoff, A.; Nurulhuda, M. Effect of substituting ZnO to ZnF_2 on Optical Properties of Nd^{3+}/Tm^{3+} Doped Tungsten-Bismuth-Tellurite Glass. *Kompleks. Ispolz. Miner. Syra = Complex Use Miner. Resour.* **2024**, *335*, 5–17. [CrossRef]

Disclaimer/Publisher's Note: The statements, opinions and data contained in all publications are solely those of the individual author(s) and contributor(s) and not of MDPI and/or the editor(s). MDPI and/or the editor(s) disclaim responsibility for any injury to people or property resulting from any ideas, methods, instructions or products referred to in the content.